

Imaging on PAPER: Centaurus A at 148 MHz

Irina I. Stefan,¹ Chris L. Carilli,² David A. Green,¹ Zaki Ali,³ James E. Aguirre,⁴ Richard F. Bradley,^{5,6,7} Dave DeBoer,³ Matthew Dexter,³ Nicole E. Gugliucci,⁷ D. E. Harris,⁸ Daniel C. Jacobs,⁹ Dave MacMahon,³ Jason Manley,¹⁰ David F. Moore,⁴ Aaron R. Parsons,^{3,11} Jonathan C. Pober¹¹ and William P. Walbrugh¹⁰

¹*Cavendish Laboratory, 19 J. J. Thomson Ave., Cambridge, CB3 0HE, UK*

²*National Radio Astronomy Observatory, Socorro, NM, USA*

³*Radio Astronomy Laboratory, University of California, Berkeley, CA, USA*

⁴*Department of Physics and Astronomy, University of Pennsylvania, Philadelphia, PA, USA*

⁵*Department of Electrical and Computer Engineering, University of Virginia, Charlottesville*

⁶*National Radio Astronomy Observatory, Charlottesville, VA, USA*

⁷*Department of Astronomy, University of Virginia, Charlottesville, VA, USA*

⁸*Smithsonian Astrophysical Observatory, Harvard-Smithsonian Center for Astrophysics, Cambridge, MA, USA*

⁹*School of Earth and Space Exploration, Arizona State University, Tempe, AZ, USA*

¹⁰*Square Kilometer Array - South Africa Project, Cape Town, South Africa*

¹¹*Astronomy Department, University of California, Berkeley, CA, USA*

¹²*Square Kilometer Array - South Africa Project, Cape Town, South Africa*

10th December 2012

ABSTRACT

We present observations taken with the Donald C. Backer Precision Array for Probing the Epoch of Reionization (PAPER) of the Centaurus A field in the frequency range 120 to 180 MHz. The resulting image has a dynamic range of 3000 and an r.m.s. of 0.5 Jy beam^{-1} . A spectral index map of Cen A is produced across the full band. The spectral index distribution is qualitatively consistent with electron reacceleration in regions of excess turbulence in the radio lobes, as previously identified morphologically. Hence, there appears to be an association of ‘severe weather’ in radio lobes with energy input into the relativistic electron population. We perform a detailed comparison of the large scale radio and X-ray emission from the ROSAT All Sky Survey. While the ROSAT field has significant gradients and structures on 10° scales possibly unrelated to Cen A, two interesting correlations are seen between the radio and X-ray emission. First is an apparent ‘cavity’ generated by the northern radio lobe on a scale of 5° , possibly indicating excavation of thermal gas by the expanding radio source. Second is a correlation between radio and X-ray ‘hot spots’ at the end of the southern lobe, some 200 kpc from the nucleus. This likely arises from Inverse Compton scattering of the CMB by the relativistic electrons also responsible for the radio synchrotron emission. The magnetic fields derived from the (possible) IC and radio emission are of similar magnitude as the minimum pressure fields, $\sim 1 \mu\text{G}$.

Key words: galaxies: individual (Centaurus A) – instrumentation: interferometers – active: galaxies – galaxies: structure – X-rays: galaxies

1 INTRODUCTION

At a distance of 3.8 Mpc (Harris, Rejkuba, & Harris 2010), Centaurus A is by far the closest radio galaxy, showing AGN-driven radio jet structures on scales from parsecs to 200 kpc (Israel 1998). Given its proximity, and very large physical scale, Cen A has become a key tool in the study of radio source physics, and radio-mode feedback in suppressing late-time gas accretion in large elliptical galaxies. However, its large angular scale ($> 10^\circ$) presents

a severe challenge to radio imaging of extended features with reasonable spatial resolution.

The last few years have seen a renaissance in low frequency radio interferometry, driven principally by the goal of studying the redshifted HI 21 cm emission from the neutral intergalactic medium during cosmic reionization over a redshift range of $6 < z < 14$, or frequency range 180 MHz to 100 MHz (Fan, Carilli, & Keating 2006; Furlanetto, Oh, & Briggs 2006; Morales & Wyithe 2010). Numerous radio interferometers are currently in operation

to study reionization, including the Murchison Widefield Array (MWA; Tingay et al. 2012), the Low-Frequency Array (LOFAR; Rottgering et al. 2006), and the Donald C. Backer Precision Array for Probing the Epoch of Reionization (PAPER; Parsons et al. 2010). In parallel to the reionization studies, the combination of good sensitivity, reasonable spatial resolution, and very wide field of view, of these interferometers presents a unique opportunity to image large-scale, non-thermal, radio continuum structures, such as those of Cen A.

Here we present the imaging results on Cen A from the PAPER array in South Africa. PAPER, with a field of view of approximately 60° , and a spatial resolution of $\sim 20''$, is ideally suited to image Cen A. In section 2 we offer a brief overview of relevant studies of Cen A. In sections 3 and 4 we review the observational techniques and describe the routine used for reducing the PAPER data. We make a detailed comparison with the higher resolution morphological analysis of Cen A at 1.4 GHz by Feain et al. (2011) in section 5. Section 6 presents the spectral index map of Cen A at 148.2 MHz. We go on in section 7 to compare the radio and X-ray structures, and show that the spectral behaviour of Cen A is consistent with particle acceleration in turbulent structures in the radio lobes. Finally, section 8 summarizes our conclusions.

2 CENTAURUS A

Centaurus A is considered the archetype of Fanaroff–Riley type I radio galaxies (i.e. edge-darkened, lower luminosity radio galaxies – usually below $2 \times 10^{25} \text{ W Hz}^{-1} \text{ sr}^{-1}$, Fanaroff & Riley 1974). Israel (1998) offers a comprehensive review of Cen A to that date.

Cen A is part of the Centaurus A/M83 Group of galaxies. The host galaxy, NGC 5128, is a massive elliptical galaxy ($M = 4.1 \times 10^{11} M_\odot$; van den Bergh 1976), with a prominent, kpc-scale dust-lane. This dust lane likely indicates a recent merger with a dusty spiral galaxy, as is also suggested by the presence of optical shells and filaments around the host galaxy (Malin, Quinn, & Graham 1983; Schiminovich et al. 1994). Stellar kinematics in the nuclear region of Cen A indicate a mass of the black hole of $M_{\text{BH}} = (5.5 \pm 3.0) \times 10^7 M_\odot$ (Cappellari et al. 2009).

At radio frequencies, early observations of Cen A revealed two giant outer lobes, extending up to 260 kpc north and south of the core, and possibly further (Cooper, Price, & Cole 1965). Subsequent imaging has delineated radio structures from sub-parsec scale jets (Tingay et al. 1998), through two well defined inner lobes and jets on scales of ~ 5 kpc (Burns, Feigelson, & Schreier 1983), as well as a ‘middle lobe’ in the northern part of the source on a scale of 30 kpc (Morganti et al. 1999).

The most comprehensive radio imaging study of the outer lobes of Cen A to date was by Feain et al. (2011). They combined observations by the Australia Telescope Compact Array and the Parkes 64 m radio telescope to image Cen A at 1.4 GHz with a spatial resolution of $\sim 50''$ over a scale of 10° . In this image, they observe a number of new features in the outer lobes. The hook-like structure at the northern-most end of the northern lobe terminates in a series of radially-centric shells with decreasing brightness. These shells have similar curvature to a diffuse filament protruding from the eastern edge of the lobe, prompting Feain et al. (2011) to suggest that both are modelled by the local group ‘weather’ (Safouris et al. 2009). Near the northeastern edge of the hook they observe a partial ring and suggest that was created by the passage of a neighbouring galaxy. In the southern lobe, Feain et al. (2011) identify a ‘vertex’ and a ‘vortex’ close to $13^{\text{h}} 20^{\text{m}}$ and $-45^\circ 15'$, which they

show could be a region of plasma reawakened by strong shocks arising from the galactic core or by the passage of a dwarf galaxy. They also remark on the detection of a turbulent Faraday rotation measure signal (Feain et al. 2009) from the southern lobe and the presence of surface wave-like structures (Bicknell, Cameron, & Gingold 1990) close to the sharply defined western edge of the lobe and suggest that, together with the ‘vertex’ and a ‘vortex’, they could be the signature of Kelvin-Helmholtz instabilities. They account for the ‘vertex’ and a ‘vortex’ being part of the wave-like structure by conjecturing a backflow dominated southern lobe with turbulent mixing.

A detailed comparison of the X-ray and radio emission on scales of order 10 kpc shows clear evidence for the interaction between the expanding radio source and the thermal cluster gas (Karovska et al. 2002). On much larger scales (~ 200 kpc), early X-ray imaging by the Ariel V satellite showed possible evidence for extended emission from the outer radio lobes (Cooke, Lawrence, & Perola 1978). Cooke, Lawrence, & Perola (1978) suggest the emission is inverse-Compton upscattering of the CMB by the relativistic electrons in the radio lobes, and calculate a radio lobe magnetic field of $0.7 \mu\text{G}$, and that this field is comparable to the equipartition field. Arp (1994), presents the ROSAT sky survey X-ray emission on a scale of 10° around Cen A. This image shows a marginal excess of X-ray emission from the end of the northern radio lobe. Stawarz et al. (2012) present the latest X-ray analysis of Cen A with the Suzaku satellite. Their spectra of lobe regions show possible diffuse emission consistent with a thermal gas in the radio lobes with a temperature 0.5 keV and density $\sim 10^{-4} \text{ cm}^{-3}$, although the very large scales involved and the relative proximity of Cen A to the Galactic plane (situated 10° to 20° off the Galactic plane) leads to some confusion in the X-ray image. If real, this thermal gas has a pressure comparable to minimum energy. We return to the X-ray-radio comparison below.

Cen A has also been studied in the > 100 GeV energy range and its radio lobes are considered a likely origin for ultra-high energy cosmic rays (Fraija et al. 2012).

3 OBSERVATIONS

PAPER is an interferometric transit array aimed at detecting the fluctuations in the 21 cm emission from the Epoch of Reionization. The project currently consists of a 32-antenna test-array situated at NRAO, in Green Bank, USA, and a 64-antenna array in South Africa’s Radio Quiet Zone¹ (latitude of approximately 30° S). The antennas are non-steerable, operate within a frequency range of 100–200 MHz and have dual linear polarization capability. The primary beam is 60° FWHM with a spatially and spectrally smooth response near to the horizon (Pober et al. 2012).

We present here data taken during one of PAPER’s observing campaigns. The data were recorded in single polarization (E–W) on four consecutive nights (3rd/4th – 6th/7th of July 2011) from approximately 4pm to 8am each ‘night’. This observing campaign offers various investigation opportunities, such as studying the Galactic Centre or searching for radio transients and Supernova Remnants. Herein we present the imaging results on Cen A.

At the time, the 64 antennas of the array were deployed in a minimum redundancy configuration (Parsons et al. 2012) within a 300 m-wide circle, with an empty central circular region of radius

¹ Further reference to PAPER will imply only the South African array.

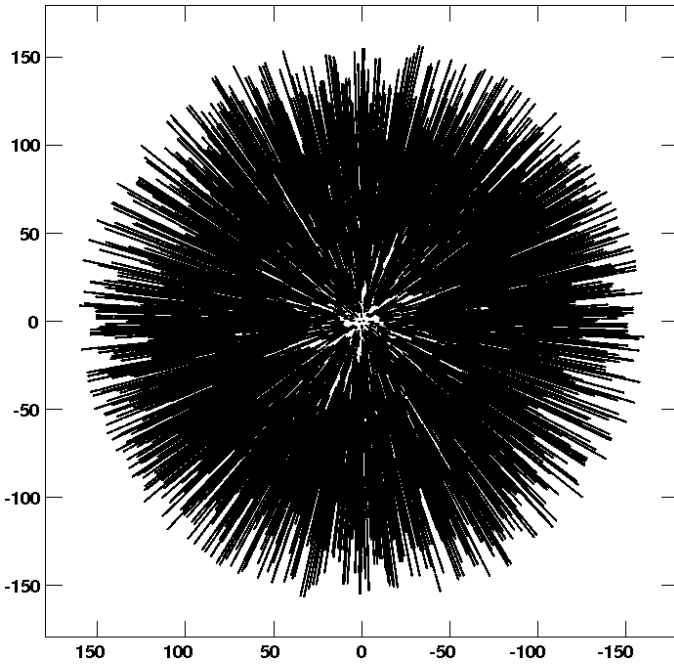


Figure 1. PAPER uv -coverage for the full band and a 10-min dataset. The axes are labelled in units of wavelength.

Table 1. Time intervals for Cen A observations.

Day	Time interval (UT)	(s)	Number of datasets
030711	16:12:35 – 18:32:53	8418	15
040711	15:54:57 – 18:25:16	9019	16
050711	16:09:09 – 18:09:25	7216	13
060711	15:46:19 – 18:16:38	9019	16

10 m. This generates a resolution of $26'$ at 145 MHz. Visibilities were integrated and recorded every 5.37 s. The full bandwidth is divided into 2048 channels, each of width 48.83 kHz. Since the antennas are not steerable, the observations were taken as a drift-scan of the sky. They were approximately continuous and divided into datasets of about 10-min long. Fig. 1 shows the uv -coverage across the full PAPER band for one 10-min dataset.

Only datasets in which Cen A was within approximately 1.5 hours from zenith are considered, as over this hour angle, the primary beam gain is approximately constant along the source track (the primary beam's gain drops by about 32% between zenith and the outermost position). Table 1 shows which time intervals were used from each night and the number of 10-min datasets used per night.

4 DATA REDUCTION

Initial pre-calibration was performed using the Astronomical Interferometry in PYthon (AIPY) package². This fixes hardware and header errors and subtracts cross-talk. An initial manual Radio Frequency Interference (RFI) excision step of the most prominently damaged channels was performed (mainly a few communication satellites bands, e.g. Orbcomm at 137 MHz). We find that due to

PAPER's location, RFI only affects a few narrow channel ranges. Frequencies below 114 MHz and above 188 MHz were flagged due to bandpass roll-off. Within each 10-min dataset, we phase tracked the mean zenith, such that the result is similar to that of a tracking interferometer and can be imaged as such.

The main calibration was carried out using the Astronomical Image Processing System (AIPS) package³. A second round of manual RFI excision was performed by inspecting the scalar averages for the total power spectra for each dataset and flagging outlying peaks. Approximately 67% of the initial data remained after both RFI excision steps. A final CLIPPING at 3 times the average visibility level ensures that any remaining outliers are removed.

Each 10-min dataset was divided into subsets of 102 frequency channels (4.98 MHz wide subsets) to mitigate bandwidth smearing effects. The 10-min time length of a dataset is sufficiently short for the effect of the source moving through PAPER's primary beam to be negligible. All subsequent steps only used baselines longer than 5 wavelengths, as the shortest baselines appear to be affected by very large scale structures which are not well sampled due to PAPER's non-uniform uv -coverage (see Fig. 1) at very short baselines (less than 10 m in length).

Given the field of view of $\sim 60^\circ$ of PAPER, the observed field cannot be approximated as a flat patch of sky anymore. We explored wide-field imaging in AIPS, which divides the field into a number of facets and cleans and images them quasi-independently. However, we found that it does not produce a much improved image, but it does significantly increase the processing time. An alternative way of tackling this problem is by w-projection (Cornwell, Golap, & Bhatnagar 2008), projecting the observed field to a tangent plane, but this technique is not available in AIPS.

The datasets were self-calibrated to obtain complex gain solutions for each antenna. Those with gain variations higher than 30% were flagged. Only four antennas had such high and unstable gains to warrant removal from at least one of the nights. The following parameters were found to give good solutions after two phase self-calibration loops and a single phase and amplitude one: a solution interval of 2 minutes, a minimum number of 5 antennas allowed for a solution and a minimum allowed signal to noise ratio of 4. Clean components were used until the first negative.

Each subset was CLEANed down to a set average flux level. This was taken to be the average root mean square noise (r.m.s.) of all the 10-min data subsets for a given night and channel range and it varied by a factor of almost 10 between the lowest and highest channel range. Imaging was performed with a restoring beam of size of $1500'' \times 1300''$, the lowest resolution across the band. A uv -weighting scheme marginally natural⁴ was found to be optimum in removing large scale effects, while still preserving enough information on the observed extended structures.

The images were normalized by the primary beam model as a function of frequency as in the survey by Jacobs et al. (2011), and resampled onto the same sky-grid, using the dataset closest to zenith as reference. For each channel range, the images corresponding to different time intervals were averaged together. We measured the flux densities of bright sources within 18.5° from zenith for each channel range and manually identified them with Culgoora sources. We eliminated sources with inconsistent historical obser-

³ <http://www.aips.nrao.edu/index.shtml>

⁴ A ROBUST factor of -1 in AIPS.

⁵ This radius was chosen such that Cen A is included in the area thus defined.

Table 3. Peak flux densities for some sources in the Cen A field as found with the JMFIT task in AIPS from an average map of the middle thirteen channel ranges. The column names are self-explanatory; the expected flux is found from the Culgoora 160 MHz measurements and the corresponding spectral indices.

Culgoora source name	Expected flux density (Jy)	Peak flux density (Jy/beam)	Rms (Jy/beam)
1221–423	8.1	7.2	0.5
1232–416	11.0	10.1	0.5
1252–289	14.9	17.1	0.5
1334–296	2.8	9.8	0.5
1355–416	29.5	31.9	0.5
1407–425	9.6	10.9	0.5
1424–418	9.9	8.3	0.5

vational data and obtained 13 sources to act as flux density calibration. We fitted spectral energy distributions (SED) to the historical data for each of these sources with quadratic functions. The flux density calibrators, their positions and their derived SED parameters are listed in Table 2. A least squares fit was performed for each channel range in order to derive scaling factors for the maps based on the calibrators’ measured and expected SEDs.

5 RESULTS

Fifteen calibrated maps were produced, one for each channel range. Fig. 2 shows a weighted average of the middle thirteen. It has a dynamic range of approximately 3000 as found from the ratio of the r.m.s. of a region near the edge of the image and the peak flux of the core of Cen A. Its r.m.s. is 0.5 Jy/beam. Cen A dominates the centre of the image and the Galactic Plane crosses it further South. The Supernova Remnant (SNR) PKS 1209–52 is visible to the SW of Cen A, at -52° Dec, as a shell with two brightened limbs (Dickel & Milne 1976).

A lower limit of 5 wavelengths was imposed for calibration and imaging, which means structures larger than 11.5° are not imaged. Very little data are eliminated this way and the negative dips in the maps evince the lack of short spacing data. Cen A is surrounded by a shallow region of negative flux. This is even more visible in and around the Galactic plane, since the Galaxy has radio emitting structures on effectively all spatial scales. Again, these negative ‘bowls’ represent missing short-spacings in the interferometric images, and result in uncertainty in the total flux measurements of large sources, and diffuse surface brightnesses. Moreover, this effect gets worse with increasing frequency, and could bias the overall spectral index distribution analysis. Hence, the spectral index discussion in section 6 will be mostly qualitative.

However, there is some evidence that Galactic emission extends all the way to Cen A (see the end of this section) and large-scale foreground emission will certainly have a significant galactic contribution. From Landecker & Wielebinski (1970), the brightness temperature in the direction of Cen A at 150 MHz is 360 K. Assuming an angular area of 12 deg^2 , the galactic foreground contribution over Cen A will be approximately 1100 Jy. So, in a way, the 11.5° angular cutoff acts as a filter for part of this emission.

Fig. 3 is a close-up view of Cen A. The core and inner lobes are saturated to show the structure in the outer lobes more clearly. The peak flux is found near $13^{\text{h}} 25^{\text{m}} 31^{\text{s}}$ and $-43^\circ 01' 26''$ to be 1631 ± 131 Jy. The integrated flux density over the entire source (taking the lowest contour level as the extent-limit for the lobes) is

3792 Jy at the average frequency of 148.2 MHz of the map. Haslam et al. (1981) found the integrated flux density of Cen A at 408 MHz to be 2762 ± 370 Jy. Assuming an average spectral index over the entire source of -0.7 between 19.7 MHz and 960 MHz (Bolton & Clark 1960), then the expected flux at 148.2 MHz is 5611 Jy. Sheridan (1958) measured Cen A’s integrated flux at 85.7 MHz to be 8700 ± 1300 Jy. Extrapolating again to 148.2 MHz gives 5929 Jy. Both of these values are significantly higher than the one measured here, stressing the importance of the missing short spaces, but neither Haslam et al. (1981) nor Sheridan (1958) correct their observations for Galactic contributions, which, again, would amount to about 1100 Jy.

The northernmost part of the southern lobe displays emission from an extended background source, the radio galaxy MRC 1318–434B (Wright & Otrupcek 1990; Smith & Bicknell 1986), associated with NGC 5090. This can be seen as a small bright patch on the northern edge of the southern lobe and dominates the measured flux density. There is a second (compact) background radio source in the centre of the southern lobe, PKS 1320–446 (Wright & Otrupcek 1990; Burgess & Hunstead 2006), but at our resolution we estimate that this source is at most 30% of the flux density measured over a single synthesized beam, and does not affect the overall analysis below.

The southern lobe shows a sharp edge along the southwestern boundary of the radio source, and more diffuse emission extending to the east in two ‘prongs’ of emission by about 2° . These two prongs are also seen at 1.4 GHz (Feain et al.). Also seen in this image is the ‘gap’ between the southern lobe and the nucleus, where the flux density drops below 7 Jy beam^{-1} (as opposed to an average of 15 Jy beam^{-1} on the northern edge of the southern lobe). This gap is also seen at 1.4 GHz.

The northern middle lobe extends outwards from the inner lobe, parallel with it, and curves northward into the outer lobe, such that the outer lobe has a position angle of approximately 0° . At about $13^{\text{h}} 28^{\text{m}}$ and $-40^\circ 33'$, the outer lobe curves east to form a hook-like structure. The northern lobe shows a general decline in flux density away from the core, with further brightening in the hook-like region at the northern end of the radio lobe, some 260 kpc from the core.

On the largest scales, faint emission may extend a few degrees beyond the two-prongs to the southeast, although missing short spacings start to become an important issue in this regard. This very extended emission to the southeast has been noted previously, and may relate to high-latitude Galactic emission, and not Cen A (Bolton & Clark 1960; Haslam et al. 1981).

6 CEN A SPECTRAL INDEX MAP

PAPER’s large bandwidth allows for spectral index maps of the observations to be computed across the band. The spectral index⁶ image is shown in Fig. 4. The spectral index was calculated at each point by taking the logarithmic difference between a weighted average image of 4 lower frequency channels (123.58 MHz – 138.38 MHz) and a weighted average of 4 higher frequency channels (158.11 MHz – 172.90 MHz). The r.m.s. of each image is used as a weight during averaging. Both images were blanked at a 5σ level. As mentioned before, incomplete reconstruction of the total flux will bias this calculation.

⁶ The convention $S = \nu^\alpha$ is used.

Table 2. The 13 sources used as flux calibrators with their Culgoora name and positions and the derived SED fit parameters. The functional form $\log_{10} S = A + B \times \log_{10} \nu + C \times \log_{10}^2 \nu$. All coordinates are in J2000.

Culgoora name	RA	Dec	A	B	C	Flux at 148.2 MHz (Jy)
1355-416	13 ^h 55 ^m 57.4 ^s	−41° 38′ 14″	8.0	−0.8	0	25.9
1308-220	13 ^h 08 ^m 57.6 ^s	−22° 00′ 33″	−16.5	5.0	0.3	67.3
1407-425	14 ^h 07 ^m 23.5 ^s	−42° 32′ 56″	15.9	−2.6	0.1	10.9
1413-364	14 ^h 13 ^m 32.3 ^s	−36° 26′ 55″	1.6	0.5	−0.1	13.3
1424-418	14 ^h 24 ^m 45.9 ^s	−41° 52′ 58″	16.9	−3.3	0.2	8.2
1421-382	14 ^h 21 ^m 11.6 ^s	−38° 13′ 29″	9.0	−1.0	0	16.9
1419-272	14 ^h 19 ^m 54.5 ^s	−27° 14′ 13″	22.2	−4.0	0.2	21.9
1422-297	14 ^h 22 ^m 32.9 ^s	−29° 47′ 06″	13.5	−2.1	0.1	17.0
1206-337	12 ^h 06 ^m 06.0 ^s	−33° 47′ 26″	−3.2	1.9	−0.2	12.8
1218-373	12 ^h 18 ^m 01.4 ^s	−37° 23′ 51″	−8.2	2.8	−0.2	8.0
1221-423	12 ^h 21 ^m 04.0 ^s	−42° 19′ 30″	−17.5	4.6	−0.3	11.0
1232-416	12 ^h 32 ^m 58.7 ^s	−41° 36′ 39″	−9.6	3.2	−0.2	9.7
1252-289	12 ^h 52 ^m 00.7 ^s	−28° 57′ 13″	5.6	0	−0.1	14.7

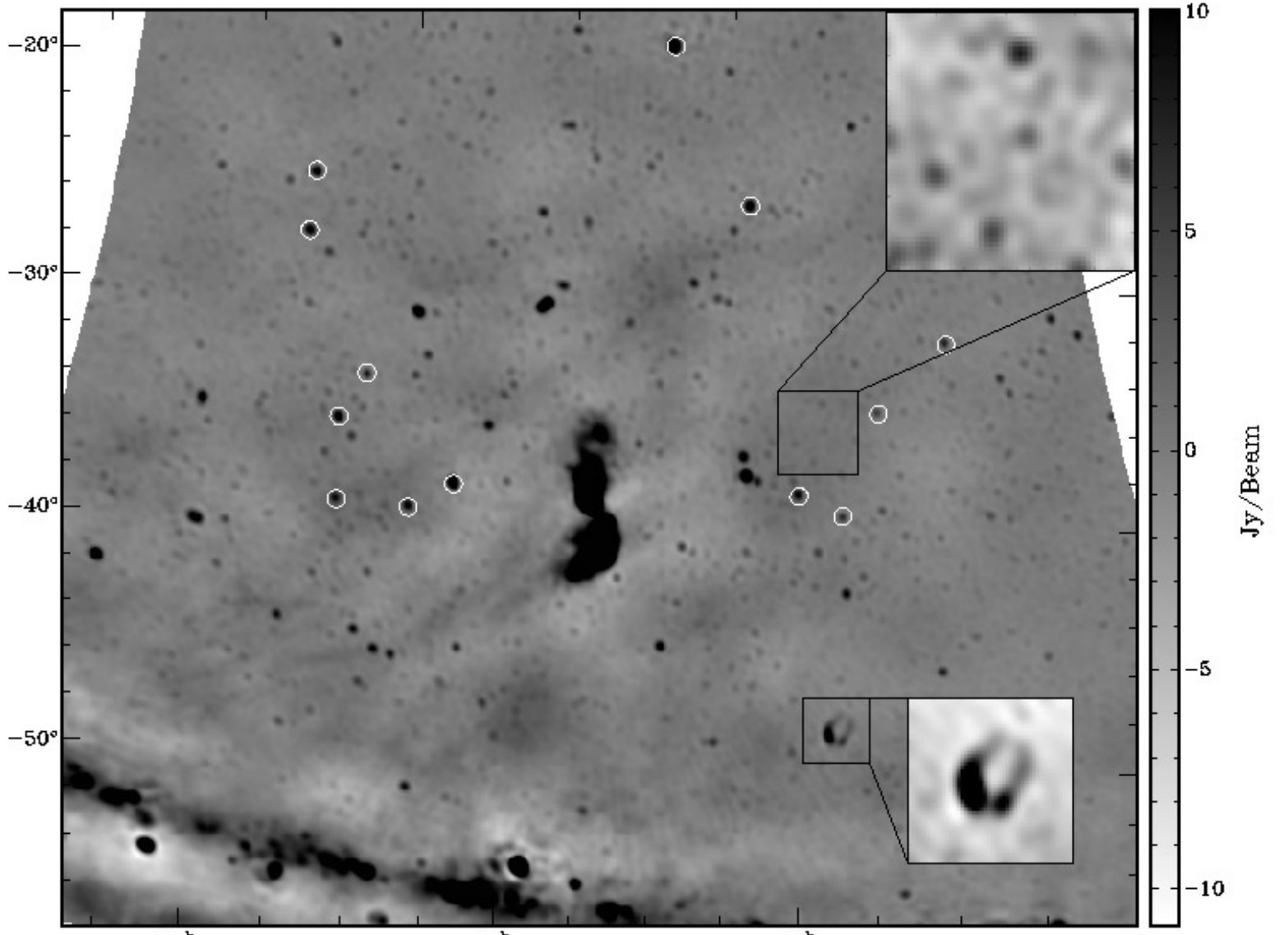


Figure 2. PAPER final image of Centaurus A obtained with a $1500'' \times 1300''$ FWHM Gaussian restoring CLEAN beam. Sources listed in Table 3 are marked with white circles. The two zoomed-in patches are on different greyscales to each other and to the general image. All coordinates are in J2000.

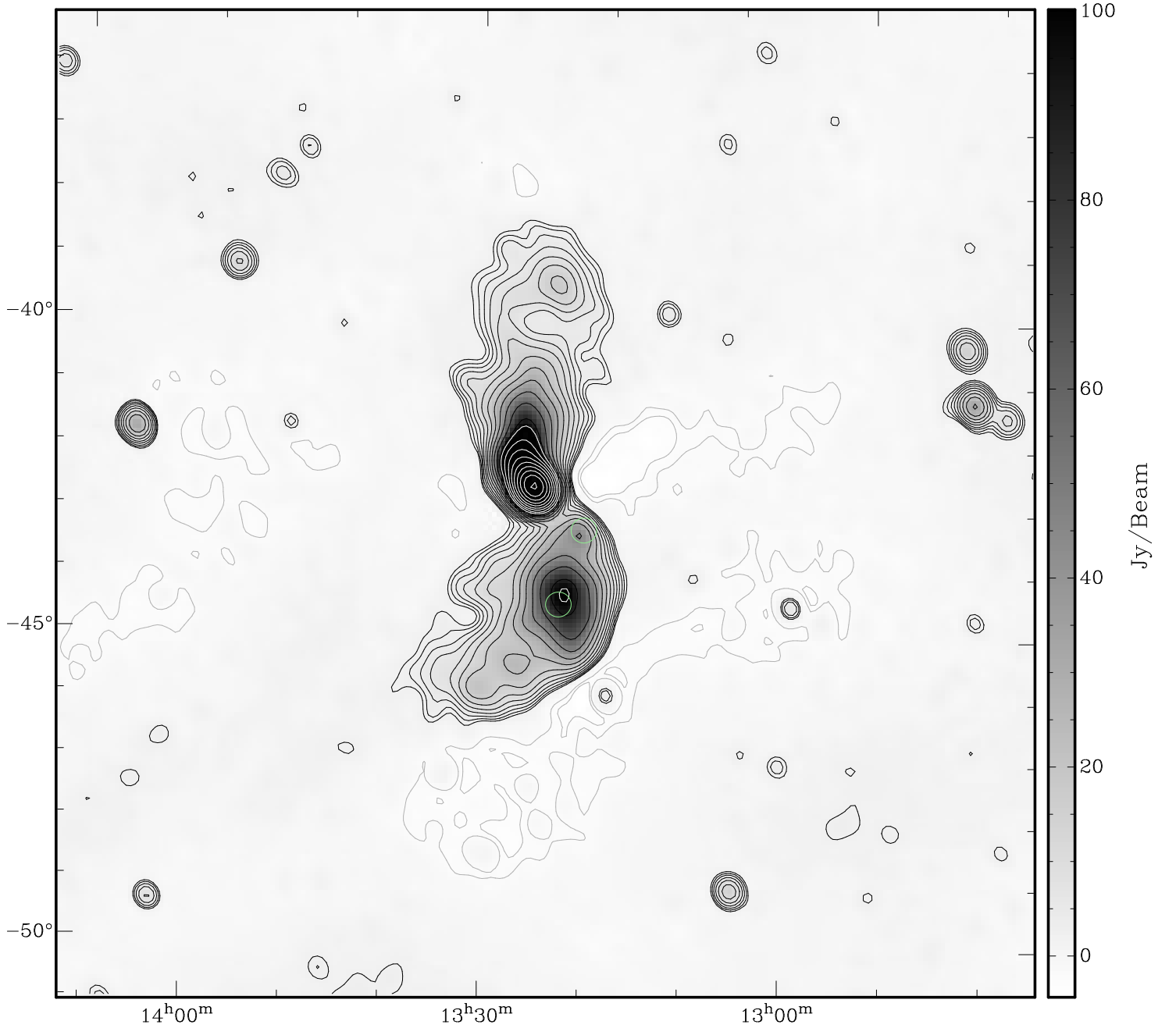


Figure 3. PAPER image of Centaurus A obtained with a $1500'' \times 1300''$ FWHM Gaussian restoring CLEAN beam. Contour levels are a geometric progression in $\sqrt{2}$, starting from 2 Jy beam^{-1} . Negative contours are in light grey. The green circles mark the positions of MRC 1318–434B and PKS 1320–446. Coordinates are in J2000.

The northern lobe shows the spectral steepening over the first 3° from the radio core, characteristic of FR I (edge-darkened) radio galaxies. Interestingly, the spectral index then becomes flatter in the northern hook-like structure, furthest from the core.

The southern lobe also shows interesting spectral behaviour. The centre of the lobe and the southwestern hard-edge show flatter spectral indices, with steepening toward the more diffuse prong to the east. And again, the very end of the southern-most prong shows flattening of the spectrum towards its tip.

The background radio galaxy on the northern edge of the

southern lobe, MRC 1318–434B, can be seen as an unresolved flatter point in the spectral index map.

7 ANALYSIS

7.1 Spectral Index

Spectral flattening in radio lobes is typically interpreted as a sign of energy input into the relativistic electron population (Carilli et al. 1991). While necessarily qualitative due to the short spacing issue,

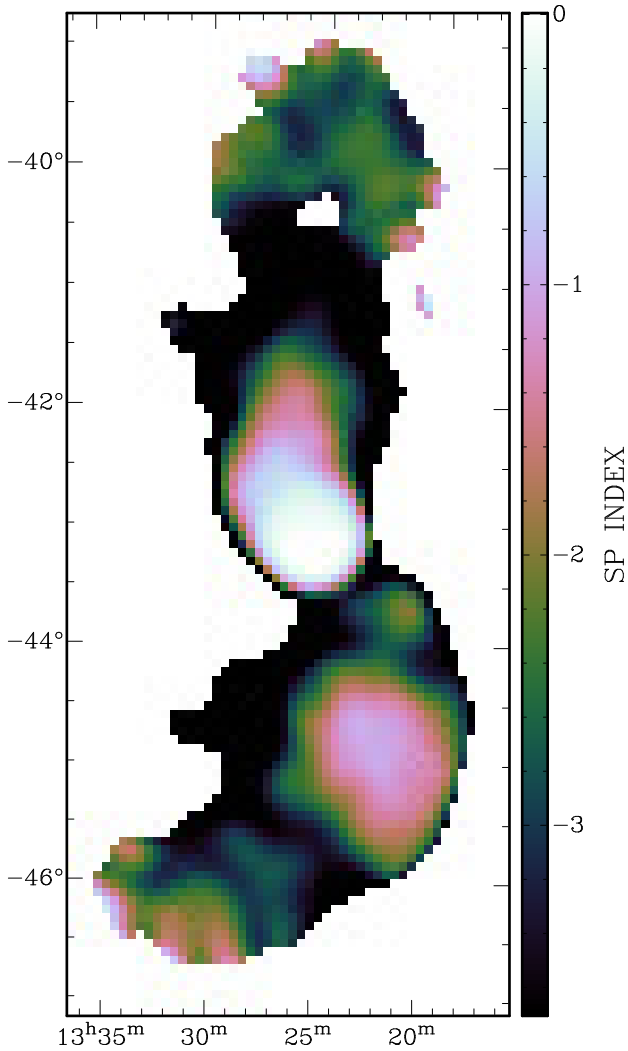


Figure 4. Spectral index map of Centaurus A. Coordinates are in J2000.

a comparison of the spectral index distribution and the morphological structures seen at high resolution, and their interpretation by Feain et al. (2011), is illustrative.

Starting with the southern lobe, we find that the central region, and the sharp southwestern edge, correspond to flatter spectral indices than the regions to the east (and close to the core, although this region is confused by a background radio source). This region is called-out explicitly in the Feain et al. (2011) analysis as being rich in high contrast, turbulent structure, notably their ‘vortex’, ‘vertex’, and ‘waves’.

Likewise, the end of the northern lobe was highlighted by Feain et al. (2011) as exhibiting multiple shells and a ring in the 1.4 GHz image. This region also shows substantial spectral flattening relative to the regions closer to the core.

The spectral flattening at the southeastern edge of the southern lobe does not correspond to equally pronounced turbulent structure in the radio images, but it does overlap with some of the X-ray emission observed in the ROSAT image (see Section 7.2).

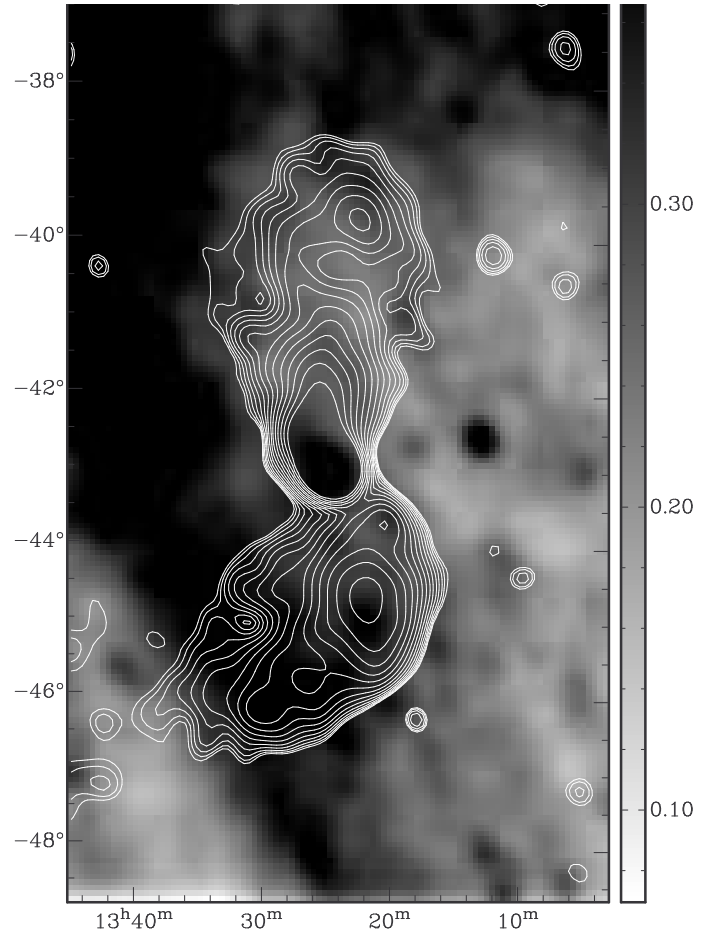


Figure 5. X-ray image of Centaurus A, taken from the ROSAT all-sky survey and smoothed with a $1500'' \times 1300''$ beam. Overlaid in white are the radio contours from 1 Jy up to 100 Jy. Coordinates are in J2000.

7.2 ROSAT All Sky Survey Comparison

Fig. 5 shows a greyscale of the 0.1 – 2.4 keV emission from the ROSAT All Sky Survey⁷ (RASS) with the PAPER Cen A contour overlaid. The X-ray image is admittedly noisy, with large gradients and clumpy structure, however, there are two interesting correlations between the radio and X-ray to note, beyond the well studied correlation on 10 kpc scales of the radio and X-ray emission from the core and inner jets.

First, in the northern lobe there appears to be a deficit of X-ray emission due to the radio lobes. This is most clearly seen along the eastern edge of the lobe. Such X-ray deficits in clusters and group X-ray halos are often seen associated with cluster radio galaxies, and likely correspond to an evacuation of the thermal cluster gas via the expanding radio source (McNamara & Nulsen 2007; Fabian 2012). This cavity would then provide a relative pressure probe of the cluster gas, given the synchrotron and IC constraints below. Unfortunately, the large X-ray filament running through the field confuses this signature. It is also possible that this large scale feature (scale of tens of degrees), running roughly north-south could be associated with high latitude Galactic emission (Stawarz et al. 2012), leading to a false deficit detection. This needs to be con-

⁷ www.xray.mpe.mpg.de/cgi-bin/rosat/rosat-survey

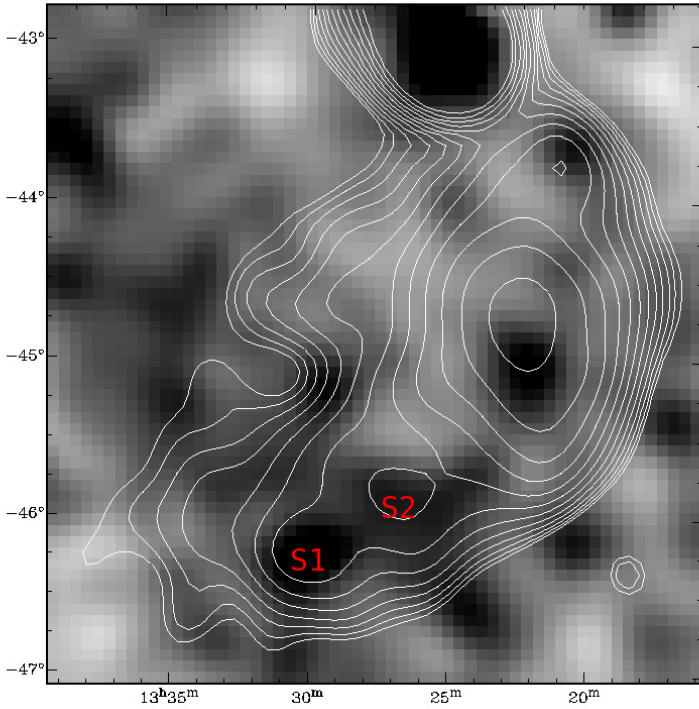


Figure 6. Close-up of the southern lobe: radio contours in white overlaid on a high pass filtered X-ray greyscale with the mean surface brightnesses at 4 times lower spatial resolution subtracted to show high contrast features. Coordinates are in J2000.

firmed through future large scale X-ray imaging of Cen A. If the deficit is indeed a cavity due to the lobe of Cen A, this would be the first direct evidence for large scale X-ray emission from the Cen A group.

More noticeable is the correlation between a series of X-ray and radio knots in the southern end of the radio source. Fig. 6 shows a close up of the region. Two X-ray knots are seen, following closely the curvature of the southern lobe and radio knots to the southeast. We have performed a pixel-pixel correlation in this region and find that the peaks correlate reasonably well, especially S1 (see Fig. 6; correlation coefficient of 0.94). Again, the ROSAT image is somewhat confused, but the correlation of the peaks and curvature of the features suggest real association.

We calculate the magnetic field strength in these regions in two ways. First, we consider minimum pressure conditions (Miley 1980), with a relativistic electron to proton ratio of $k = 1$, unity filling factor, upper and lower frequency cutoffs for the radio spectrum of 10 MHz and 10 GHz and a luminosity distance of 3.75 Mpc. We assume that the emission is coming from a spherical region in the lobe of $15'$ radius. The resulting fields are given in Table 4. The values range from $0.5 \mu\text{G}$ to $1 \mu\text{G}$, depending on the spectral index assumed.

Second, we consider that the X-ray emission is due to inverse Compton upscattering of the ambient CMB photons (the dominant photon field in the outer lobe regions) by the synchrotron emitting relativistic electrons (Harris & Grindlay 1979; Miley 1980). The X-ray luminosity was determined after convolving the counts to $15'$ resolution, and subtracting a background based on an annulus with the same area as the photometric circle. The resulting X-ray luminosities and magnetic fields are given in Table 4. We find fields

Table 4. Magnetic field strengths found from the RASS X-ray image. $L_{\text{X-ray}}$ is the measure X-ray luminosity, B_{minP} the magnetic field strength found through the minimum pressure condition and B_{IC} the magnetic field strength found through assuming inverse Compton scattering. S1 and S2 are marked in Fig. 6 and α is the spectral index. We use two values for the spectral index to account for the uncertainty in the absolute α measured from Fig. 4.

	S1		S2	
	$\alpha = -1$	$\alpha = -1.8$	$\alpha = -1$	$\alpha = -1.8$
$\log(L_{\text{X-ray}}(\text{erg s}^{-1}))$	39.0	39.2	39.9	40.1
$B_{\text{minP}}(\mu\text{G})$	0.56	0.80	0.67	0.96
$B_{\text{IC}}(\mu\text{G})$	0.25	1.25	0.12	0.74

between $0.1 \mu\text{G}$ and $1.3 \mu\text{G}$, again depending on the spectral index. In general, the fields based on a minimum pressure assumption and those based on inverse-Compton emission are of similar magnitude.

Hardcastle et al. (2009) find an upper limit for the density of the X-ray emitting gas in Cen A's lobes of 10^{-4} cm^{-3} , which agrees with the value range derived by Stawarz et al. (2012). Assuming $n_g = 10^{-4} \text{ cm}^{-3}$ and a gas temperature of $kT \sim 0.5 \text{ keV}$ (as found by Stawarz et al. 2012), then the lobes' thermal pressure is approximately $8 \times 10^{-14} \text{ erg cm}^{-3}$. Stawarz et al. (2012) found that this thermal pressure counterbalances the pressure of a non-thermal plasma ($8 \times 10^{-14} \text{ erg cm}^{-3}$) with an average magnetic field of strength $B \sim 1 \mu\text{G}$ in rough equipartition with ultra-relativistic electrons. It is encouraging that the magnetic field strength required for pressure balance of the different plasma species is of the same order as the average magnetic field strength we find for the Cen A lobes, $B \sim 1 \mu\text{G}$.

8 CONCLUSIONS

We present wide field imaging of large scale structures taken with the Precision Array for Probing the Epoch of Reionization in the frequency range 120 to 180 MHz of the closest radio galaxy, Centaurus A, and a comparison to the large scale X-rays.

We observe a correspondence between regions rich in complex morphological radio structure at 1.4 GHz (described by Feain et al. 2011) and regions of flatter spectral index in our 148.2 MHz maps. The northern loop of the northern lobe, where Feain et al. (2011) show a series of shells and a ring, sees a flattening of the spectral index relative to the regions closer to the core. Similar flattening is seen in the central and western part of the southern lobe, where Feain et al. (2009) observe a 'vertex' and a 'vortex'. This likely indicates active particle acceleration on large scales in the radio lobes, through supersonic turbulences. We note that the gap between the core of the galaxy and the northern edge of the southern lobe, which has also been observed at 1.4 GHz (Feain et al. 2011), is still seen at 148.2 MHz.

Considering the RASS comparison, the end of the southern lobe shows a correlation of X-ray emission with a series of radio knots seen in the 148.2 MHz PAPER image. Assuming this is inverse Compton up-scattering of the CMB by the synchrotron emitting relativistic electrons, we find that the magnetic field strengths required are comparable to the ones found from the ROSAT image, assuming a spherical emission region embedded in the southern lobe. Also, fields of the order of $1 \mu\text{G}$ are found across both lobes from the radio map assuming minimum energy conditions. Assuming an average minimum energy of ultra-relativistic electrons of $4 \times 10^{-14} \text{ erg cm}^{-3}$ and cylindrical symmetry for Cen A (radius 2° and height 4°), we find the total non-thermal energy stored in the

lobes to be 1.7×10^{58} erg. The possible cavity seen in the northern lobe due to the expanding radio source provides a rough measure of the thermal pressure in the cluster, via balance with minimum energy pressures in the lobes.

ACKNOWLEDGMENTS

We thank the SKA project office in South Africa for their efforts in ensuring the smooth running of PAPER. The PAPER project is supported through the NSF-AST program (award 0804508), and by significant efforts by staff at NRAO's Green Bank and Charlottesville sites. We have made use of the ROSAT Data Archive of the Max-Planck-Institut für extraterrestrische Physik (MPE) at Garching, Germany.

References

- Abdo A. A., et al., 2010, *Sci*, 328, 725
 Alvarez H., Aparici J., May J., Reich P., 2000, *A&A*, 355, 863
 Arp H., 1994, *A&A*, 288, 738
 Bicknell G. V., Cameron R. A., Gingold R. A., 1990, *ApJ*, 357, 373
 Bolton J. G., Clark B. G., 1960, *PASP*, 72, 29
 Burbidge G. R., 1959, *ApJ*, 129, 849
 Burgess A. M., Hunstead R. W., 2006, *AJ*, 131, 114
 Burns J. O., Feigelson E. D., Schreier E. J., 1983, *ApJ*, 273, 128
 Burtscher L., Meisenheimer K., Jaffe W., Tristram K. R. W., Röttgering H. J. A., 2010, *PASA*, 27, 490
 Cappellari M., Neumayer N., Reunanen J., van der Werf P. P., de Zeeuw P. T., Rix H.-W., 2009, *MNRAS*, 394, 660
 Carilli C. L., Perley R. A., Dreher J. W., Leahy J. P., 1991, *ApJ*, 383, 554
 Cooke B. A., Lawrence A., Perola G. C., 1978, *MNRAS*, 182, 661
 Cooper B. F. C., Price R. M., Cole D. J., 1965, *AuJPh*, 18, 589
 Cornwell T. J., Golap K., Bhatnagar S., 2008, *ISTSP*, 2, 647
 Fabian A. C., 2012, *ARA&A*, 50, 455
 Fan X., Carilli C. L., Keating B., 2006, *ARA&A*, 44, 415
 Fanaroff B. L., Riley J. M., 1974, *MNRAS*, 167, 31P
 Feain I. J., et al., 2009, *ApJ*, 707, 114
 Feain I. J., et al., 2011, *ApJ*, 740, 17
 Fraija N., González M. M., Perez M., Marinelli A., 2012, *ApJ*, 753, 40
 Furlanetto S. R., Oh S. P., Briggs F. H., 2006, *PhR*, 433, 181
 Dickel J. R., Milne D. K., 1976, *AuJPh*, 29, 435
 Hardcastle M. J., Cheung C. C., Feain I. J., Stawarz Ł., 2009, *MNRAS*, 393, 1041
 Harris D. E., Grindlay J. E., 1979, *MNRAS*, 188, 25
 Harris G. L. H., Rejkuba M., Harris W. E., 2010, *PASA*, 27, 457
 Haslam C. G. T., Klein U., Salter C. J., Stoffel H., Wilson W. E., Cleary M. N., Cooke D. J., Thomasson P., 1981, *A&A*, 100, 209
 Israel F. P., 1998, *A&ARv*, 8, 237
 Jacobs D. C., et al., 2011, *ApJ*, 734, L34
 Junkes N., Haynes R. F., Harnett J. I., Jauncey D. L., 1993, *A&A*, 269, 29
 Karovska M., Fabbiano G., Nicastro F., Elvis M., Kraft R. P., Murray S. S., 2002, *ApJ*, 577, 114
 Landecker T. L., Wielebinski R., 1970, *AuJPA*, 16, 1
 Malin D. F., Quinn P. J., Graham J. A., 1983, *ApJ*, 272, L5
 McNamara B. R., Nulsen P. E. J., 2007, *ARA&A*, 45, 117
 Miley G., 1980, *ARA&A*, 18, 165
 Morales M. F., Wyithe J. S. B., 2010, *ARA&A*, 48, 127
 Morganti R., Killeen N. E. B., Ekers R. D., Oosterloo T. A., 1999, *MNRAS*, 307, 750
 Parsons A. R., et al., 2010, *AJ*, 139, 1468
 Parsons A., Pober J., McQuinn M., Jacobs D., Aguirre J., 2012, *ApJ*, 753, 81
 Pober J. C., et al., 2012, *AJ*, 143, 53
 Pritchard J. R., Loeb A., 2011, *arXiv:1109.6012*
 Röttgering H. J. A., et al., 2006, *astro*, *arXiv:astro-ph/0610596*
 Safouris V., Subrahmanyan R., Bicknell G. V., Saripalli L., 2009, *MNRAS*, 393, 2
 Sheridan K. V., 1958, *AuJPh*, 11, 400
 Schiminovich D., van Gorkom J. H., van der Hulst J. M., Kasow S., 1994, *ApJ*, 423, L101
 Smith R. M., Bicknell G. V., 1986, *ApJ*, 308, 36
 Stawarz Ł., et al., 2012, *arXiv*, *arXiv:1210.4237*
 Tingay S. J., et al., 2012, *arXiv*, *arXiv:1206.6945*
 Tingay S. J., et al., 1998, *AJ*, 115, 960
 van den Bergh S., 1976, *ApJ*, 208, 673
 Wright A., Otrupcek R., 1990, *PKS*, 0